ACS Catalysis

pubs.acs.org/acscatalysis

Research Article

Elucidating the Significance of Copper and Nitrate Speciation in Cu-SSZ-13 for N_2O Formation during NH_3-SCR

Leila Negahdar,* Naomi E. Omori, Matthew G. Quesne, Mark D. Frogley, Fernando Cacho-Nerin, Wilm Jones, Stephen W. T. Price, C. Richard A. Catlow, and Andrew M. Beale*

Cite This: *ACS Catal.* 2021, 11, 13091−13101

Read Online

ACCESS | Metrics & More | Article Recommendations | Supporting Information

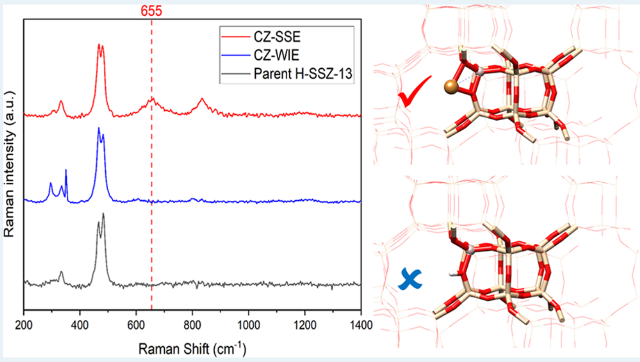

ABSTRACT: Unwanted N_2O formation is a problem that has been noted in selective catalytic reduction (SCR) where copper zeolite catalysts are utilized. With its immense global warming potential and long-term stability, elevated atmospheric N_2O has already been identified as a future challenge in the war on climate change. This paper explores the phenomenon of N_2O formation during NH_3-SCR over Cu-SSZ-13 catalysts, which are currently commercialized in automotive emissions control systems, and proposes a link between N_2O production and the local copper environment found within the zeolite. To achieve this, a comparison is made between two Cu-SSZ-13 samples with different copper co-ordinations produced via different synthesis methods. A combination of synchrotron X-ray absorption near-edge spectroscopy, UV−vis, Raman, and density functional theory (DFT) is used to characterize the nature of copper species present within each sample. Synchrotron IR microspectroscopy is then used to compare their behavior during SCR under *operando* conditions and monitor the evolution of nitrate intermediates, which, along with further DFT, informs a mechanistic model for nitrate decomposition pathways. Increased N_2O production is seen in the Cu-SSZ-13 sample postulated to contain a linear Cu species, providing an important correlation between the catalytic behavior of Cu-zeolites and the nature of their metal ion loading and speciation.

KEYWORDS: *Cu-zeolites, NH_3-SCR, NO_x, operando IR, XAFS, DFT calculation, mechanism*

1. INTRODUCTION

Selective catalytic reduction (SCR), also referred to as deNO_x technology, is a commercialized catalytic reaction used in combustion engines to convert unwanted nitrogen oxides into a benign mixture of nitrogen gas and water. NO_x gases are pollutants that pose a hazard to human respiratory functions and environmental ecosystems.[1] Almost 50% of NO_x emissions originate from combustion engines used in transport, with a further 20% arising from the stationary production of energy such as thermal power plants and industrial boilers.[2] To address this, SCR, which has been shown to reduce NO_x emissions by as much as 95%,[3] is currently used in diesel engine cars and trucks to meet emissions standards in Europe (Euro6), US (EPA Tier 2 and 3), and Southeast Asia.

SCR occurs when NO_x gases are flowed through an appropriately selected catalyst in the presence of a reductant such as ammonia. In SCR, it is important to match the right catalytic material to the operational environment the reaction will be performed under, considering factors like temperature and humidity. Small pore Cu-zeolites have been identified as excellent catalysts in the SCR reaction, being lauded for their unrivaled NO_x conversion.[4−6] Additionally, their strong performance in the highly topical low-temperature SCR (LT-SCR) region (i.e., ≤350 °C)[7,8] and durability following hydrothermal aging[9] make them excellent candidates for vehicular SCR and the current catalysts of choice for commercialized SCR in heavy goods diesel vehicles.[10]

An issue that is becoming increasingly recognized is the unwanted formation of N_2O during SCR where small pore Cu- and Fe-zeolites are used as catalysts.[11−14] A similar phenomenon has also been observed when Mn-Fe spinels,[15] V_2O_5-WO_3/TiO_2,[16] and Mn/Ti-Si[17] are used as the catalyzing agent. Although historically exempt from emissions regulations due to their believed lack of toxicity, harmful indications following long-term exposure[18] and a global warming potential almost 300 times that of CO_2[19] mean that N_2O will inevitably become the subject of increasingly exacting legislation beyond

Received: July 14, 2021
Published: October 13, 2021

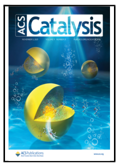

https://doi.org/10.1021/acscatal.1c03174
ACS Catal. 2021, 11, 13091−13101

emissions standards. While pronounced formation of N_2O has been experimentally observed previously, the mechanism by which this occurs is not completely understood and it is likely there is some degree of catalyst dependency. In Cu-zeolite systems, N_2O formation mechanisms have broadly been associated with nonselective catalytic reduction (NSCR) and nonselective NH_3 oxidation (NSNO) pathways,[12,20] as well as additional SCR side reactions[21] and the decomposition of NH_4NO_3 to form N_2O and water.[22−25] Liu et al.[12] and Zhang et al.[11] posited in a study of Cu-SSZ-13 that N_2O formation mechanisms were temperature-dependent, occurring at low temperatures due to the decomposition of nitrates formed preferentially on $Cu(OH)^+$ complexes thought to exist within Chabazite zeolites (CHA) cages as Lewis sites and at high temperatures due to NH_3 oxidation by O_2 and NO_x. Kamasamudram et al.[13] in their study of Cu-zeolites also identified differences in N_2O selectivity as a function of temperature noting that peak production seemed to occur at around 300 °C in what would be considered the LT-SCR region, which they also attributed to the decomposition of surface ammonium nitrate species. They also noted a relationship with copper loading where higher concentrations of copper were associated with higher rates of N_2O formation, especially in the low-temperature region. Structural considerations were raised by Kwak et al. who noted that N_2O production was framework-dependent with Cu-ZSM-5, Cu-β, and Cu-Y all forming larger amounts of N_2O than Cu-SSZ-13 under the same conditions.[26] Specifically, in Cu-β, they also observed elevated N_2O production in a hydrothermally aged sample, which was also observed by Lee et al. in Cu-UZM-35.[27]

While the effect of temperature has been well established, less certain is the precise effect of copper speciation on N_2O formation. The widely reported disparity in N_2O production based on the framework type implies that not just the structure but the availability of certain copper co-ordination environments is crucially important in the formation of nitrate species at low temperatures. This paper aims to explore in greater depth the relationship between the copper environment of the Cu-zeolite catalyst and its propensity for N_2O formation. This is achieved by comparing Cu-SSZ-13 samples prepared by two different methods thought to induce the formation of different copper species within the framework: the first synthesized via a standard wet ion-exchange method known to produce an efficient SCR catalyst material[28] and the second prepared by a solid-state incorporation method. In particular, the presence of copper aluminate species, which has previously been associated with the deactivation of Cu-zeolites,[29−31] is considered as a site for preferential nitrate formation.

To demonstrate this correlation, the samples were studied using an ambitious combination of two synchrotron techniques at the diamond light source. The hard X-ray nanoprobe on beamline I14 was used to generate X-ray fluorescence (XRF) and X-ray absorption near-edge structure (XANES) maps, providing detailed, spatially resolved information on the nature of copper speciation within each sample, setting a high benchmark for the characterization of the catalysts. The multimode infrared imaging and microspectroscopy (MIRIAM) beam on B22, differentiated by its high brilliance irradiation source and superior signal to noise, was then used to identify vibrational modes of nitrate components under operando conditions. Furthermore, density functional theory (DFT) using a quantum mechanics/molecular mechanics (QM/MM) approach was employed to elucidate the reaction pathway for formation of N_2O over the Cu-SSZ-13 catalyst. It is envisioned that the proposed mechanism for N_2O formation based on experimental evidence will facilitate the rational design and development of efficient catalysts for use in future practical NH_3-SCR in systems.

2. MATERIALS AND METHODS

2.1. Sample Preparation. A parent SSZ-13 zeolite (Si/Al = 13) was synthesized using *N*,*N*,*N*-trimethyladamantammonium hydroxide as a structural directing agent in a fluoride medium, under static hydrothermal conditions.[32,33] The proton form of the zeolite was obtained by calcining the sample in air by heating at 1 °C min^{-1} to 120 °C, held for 2.5 h and then at 4 °C min^{-1} to 550 °C, held for 10 h. Copper-exchanged forms of the zeolite were created via the following two preparations. The first method was a wet ion-exchange method, as reported previously.[34] An amount of the H-SSZ-13 was added to an aqueous solution of copper sulfate and heated at 80 °C for 2 h under stirring. The product was recovered by vacuum filtration, washed with copious amounts of water, dried overnight at 80 °C, and calcined in air. This sample is hereafter referred to as "Cu-Zeolite Wet Ion Exchange" (CZ-WIE). Crystals used for the CZ-WIE preparation were on average 8 μm in diameter. The second method was a solid ion-exchange preparation. Cu-nitrate was combined in a five-time stoichiometric excess with the H-SSZ-13 framework (five-times Cu content with respect to the Al amount in the zeolite) in a mortar and pestle and mechanically incorporated. The resultant sample was filtered and dried at 120 °C overnight, before being calcined again at 550 °C with a ramp rate of 2 °C min^{-1}. This sample is hereafter referred to as "Cu-Zeolite Solid State Exchange" (CZ-SSE). To ensure consistent and reproducible results during the study, both calcined zeolite samples were further hydrothermally treated at 650 °C for 4 h in synthetic air containing 5% H_2O prior to experimentation. Crystals used for the CZ-SSE preparation were on average 2 μm in diameter. The resultant samples featured a Cu loading of 3 wt % analyzed by SEM-EDX (Tables S2 and S3).

2.2. UV−Vis Diffuse Reflectance. UV−vis spectra were acquired under ambient conditions with a Shimadzu 2700 UV−vis spectrophotometer fitted with an optical integrating sphere for solid powdered samples. Zeolites were pressed into a sample holder and mounted vertically in the integrating sphere. A standard barium sulfate ($BaSO_4$, Sigma-Aldrich, 99%) sample was used for baseline scans. Spectra were collected from 200−1400 nm on a slow scan speed and a resolution of 0.5 nm.

2.3. Raman Spectroscopy. Raman spectra were obtained from an InVia confocal Raman microscope (Renishaw, Wotton-under-Edge, UK) equipped with a 50× objective lens (Nikon, L Plan Apo, 50×/0.45, WD17) and Peltier cooled CCD. The sample was irradiated with either an 830 nm diode laser with the 34 mW maximum power output or a 514 nm Stellar PRO argon laser (Modu-laser) with the 10 mW maximum power output. Attenuated laser power at the sample was achieved using neutral density filters. A grating with 1200 lines/mm was used, yielding an overall spectral resolution of 1 cm^{-1}. A three-point FFT filter has been applied to the spectrum.

2.4. *Operando* IR Spectroscopy. A Bruker Hyperion 3000 infrared microscope fitted with a 36× magnification objective and condenser coupled to a Bruker Vertex 80V FTIR

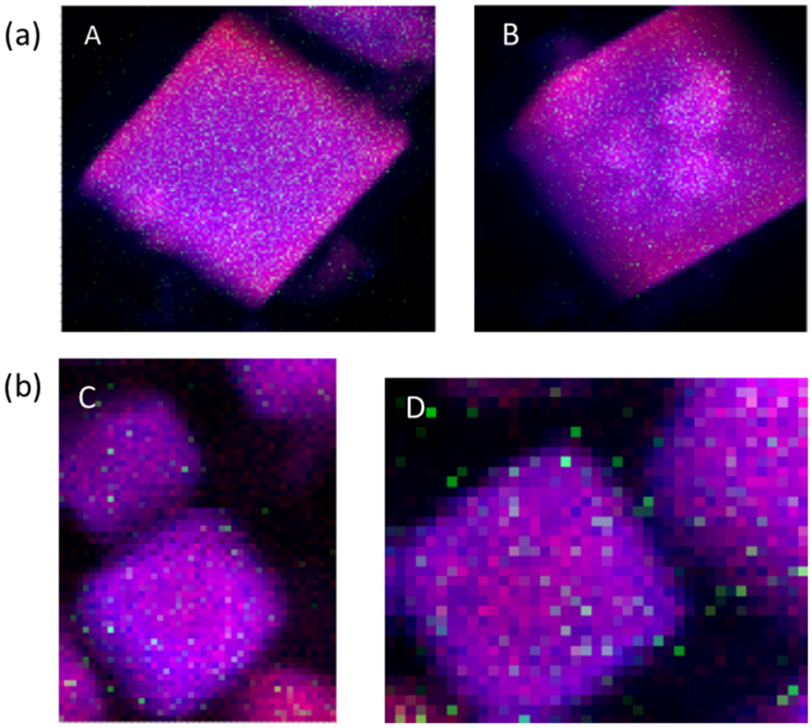

Figure 1. Nano-XRF images of copper SSZ-13 catalysts prepared by two different ion-exchange methods. (a) Nano-XRF (step size = 100 nm, detector 0.05) elemental map of CZ-WIE showing silicon (red) and copper (blue), b) nano-XRF (step size = 100 nm, detector 0.05) elemental map of CZ-SSE showing silicon (red) and copper (blue); the field of view (FOV) in these images is A and B: 14 μm squared, C and D: 4 × 6 μm and 4 × 4 μm, respectively.

instrument at MIRIAM beamline B22 of Diamond Light Source was used to acquire IR spectra. A slit size of 25 × 25 μm^2 and a beam size of 10 × 10 μm^2 was used. Bulk transmission IR experiments were performed on 6 mm diameter wafers of catalyst particles (~10 mg), which were formed by pressing at a pressure of 1.5 ton cm^{-2} for 1 min. Wafers were placed onto a CaF_2 window mounted inside a temperature-controlled Linkam FTIR600 reaction cell. Gas stream inlets to the cell were controlled by a mass flow controller. Prior to experimentation, wafers were dehydrated by heating at 300 °C under a nitrogen atmosphere 100 mL min^{-1} N_2 flow. When adsorbed water bands were no longer visible in the spectrum, the Linkam cell was cooled down to the desired reaction temperature under N_2 flow at a rate of 10 °C min^{-1}. Spectra were recorded from selected points across the sample with 256 scans and 4 cm^{-1} resolutions, equivalent to 32 s per measurement, using the Bruker OPUS software. NH_3-SCR was performed using a "standard" gas mixture of 500 ppm NO, 500 ppm NH_3, and 1000 ppm O_2 (balance N_2) at 180 °C. The outlet of the cell was connected to a Portable quadrupole mass spectrometer (ECOSYS) to provide qualitative information for reactant consumption and product formation.

2.5. X-ray Fluorescence (XRF) and X-ray Absorption Near-Edge Spectroscopy (XANES). Nano-XRF and nano-XANES experiments were performed in the Hard X-ray Nanoprobe beamline at Diamond Light Source. The sample was suspended in isopropanol and drop-cast on a silicon nitride membrane (Silson Ltd.), which was subsequently mounted on a dedicated sample holder available at the beamline. The sample was scanned across the X-ray beam using a focal spot of 100 nm (FWHM) and matching step size, to form an image with the 100 nm lateral resolution. At each point in the image, a full XRF spectrum was collected using a four-element silicon-drift detector. Nano-XRF images were obtained at a photon energy, selected to excite Si, Al, and Cu fluorescence. Nano-XANES images were obtained by acquiring successive nano-XRF images at ~100 photon energies crossing the K absorption edge of Cu (8.979 keV). Once acquired, the XRF spectrum at each point was integrated over a constant energy window corresponding to the Cu Kα emission, resulting in a series of images. These were co-aligned and cropped to correct for drift and inaccuracy from the motion platform, resulting in a stack containing one image layer per photon energy of the XANES scan. Principal component analysis and clustering were then applied to the resulting stack using the freely available package HyperSpy.[35] The sum spectrum corresponding to all points within a cluster was extracted and analyzed with the freely available package Athena.[36]

2.6. IR Transmission Spectroscopy. The IR transmission cell was a Harrick temperature-controlled gas cell, with a path length of 10 cm, a volume of 17 cm^3, and CaF_2 windows. The IR spectrometer was a Thermo Scientific, Nicolet iS10. Twenty milligrams of the catalyst powder was placed into the Harrick Praying Mantis high-temperature reaction cell. Gas stream inlets to the reaction cell were controlled by a mass flow controller and spectra were recorded every 1 min. NH_3-SCR was performed using a gas flow of 10 mL min^{-1} of NO, 10 mL min^{-1} of NH_3, and 80 mL min^{-1} of O_2 (a gas mixture of 1000 ppm NO, 5000 ppm NH_3, and 8000 ppm O_2) at 180 and 250 °C.

2.7. Periodic DFT Models and QM/MM Models. The periodic DFT calculations followed well-established and benchmarked protocols,[37] with the intermediate structures generated by modifying the aforementioned crystal structure coordinates to include copper aluminate as well as the important nitrogenous species. QM/MM protocols utilizing the ChemShell code[38,39] as a platform to simulate adsorption and vibrational properties of both protonated and metal-containing zeolitic aluminosilicates have demonstrated excellent convergence between experimentally derived values and those obtained by the embedded cluster models.[40,41] Therefore, such a scheme was used in this study, whereby, the unit cell of CHAμ was extended to a sphere of 25 Å in radius around the acid site and the charge compensating proton was exchanged for a copper cation. Detailed information on this section can be found in the Supporting Information.

3. RESULTS AND DISCUSSION

3.1. Nano-XRF and Nano-XANES. Nano-XRF and -XANES analysis was conducted to establish the nature and distribution of copper species across each SCR catalyst. XANES is used to establish the presence of an aluminate phase in the CZ-SSE preparation. Overlaid XRF elemental maps of silicon (red), aluminum (green), and copper (blue) acquired with the 100 nm resolution are shown in Figure 1, which show representative crystals from the CZ-WIE (top) and CZ-SSE (bottom) batch. CZ-WIE shows a relatively uniform distribution of copper across the sample and thin regions of copper depletion on the crystal edges where the silicon map appears more pronounced. Copper distribution is expected to be even across the sample during the wet ion-exchange preparation method, which sees copper starting in solution as Cu^{2+} hexa-aqua ions and being drawn in a sponge-like fashion into the porous structure when water ligands are dropped during dehydration. Conversely, in the CZ-SSE sample, the copper appears to be zoning around the edge of the crystal, with a region of copper depletion instead being present in the center of the crystal. This can be attributed to the synthesis method of mechanical incorporation, which forces ion exchange to occur in the solid state almost exclusively via surface diffusion.

Figure 2 shows the average Cu-XANES spectra for the CZ-WIE (black) and the CZ-SSE (red) samples. Cluster analysis of the XANES maps showed that for both samples, one significant XANES spectrum could be extracted. This indicates that although there is a clear difference between the copper speciation of each sample, there is limited variation in copper speciation within each sample as a function of spatial variation.

In total, four features of interest have been identified, all of which have been previously assigned by Deka et al.[30] Feature 1, expanded for clarity between 8975 and 8980 eV, is assigned to dipole forbidden 1s → 3d transition in Cu^{2+}. The feature is present in both samples but shifted from 8977 eV in the CZ-SSE sample to 8978 eV in the CZ-WIE sample. Feature 2 at 8982 eV is associated with the 1s orbital to double degenerate $4p_{xy}$ transitions in linear Cu^{+} systems like $CuAlO_2$.[30,42−4430,42−44] Although present in both samples, the feature is much more prominent in the Cu-SSE sample indicating a higher concentration of Cu^{+} species. Feature 3 at 8986 eV is only seen in CZ-WIE and is associated with a Cu^{2+} 1s → 4pz ligand Cu^{2+} charge transfer. Feature 4: 8995 eV is seen in both samples. The difference can also be seen in the tail of the spectra. CZ-SSE appears to be experiencing a frequency shift relative to the CZ-WIE sample that is consistent with the longer bond length associated with Cu^{+} systems. Finally, it is worth noting that feature 4 highlights a drop in the rising absorption edge intensity and hence the difference in the number of unoccupied electronic states of the absorber atom in each catalyst. Overall, XANES indicates that both samples are exhibiting multiple copper environments. However, a side-by-side comparison of the two catalysts shows considerable differences in the intensity ratios of all of the edge-features discussed. In particular, the prominence of feature 2 indicates that there is more Cu^{+} in the CZ-SSE sample than the CZ-WIE sample. Additionally, the Cu-SSE sample is in good agreement with a Cu-SSZ-13 zeolite previously shown to have an aluminate phase present.[30] It is worth noting that although Deka et al. used a vapor deposition method to create an aluminate-rich catalyst, solid-state exchange is generally a more systematic preparation method as vapor deposition is known to have problems with gradients of copper impregnation across the zeolite bed.[30]

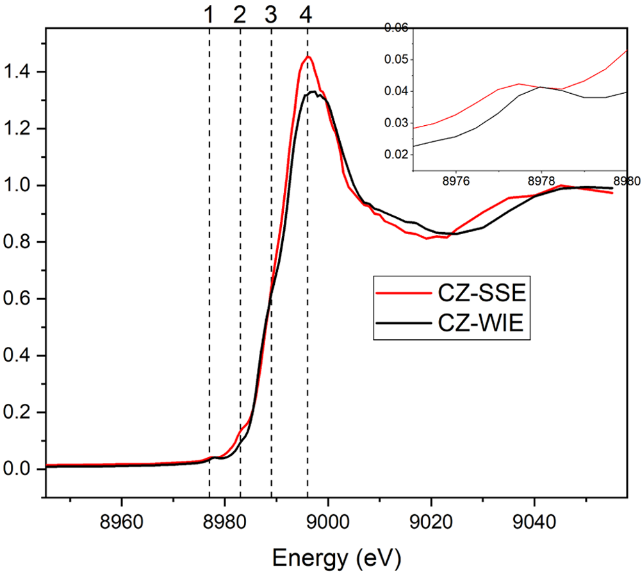

Figure 2. Normalized average XANES spectra of CZ-WIE and CZ-SSE. Feature 1 at 8975−8980 eV; feature 2 at 8982 eV; feature 3 at 8986 eV; and feature 4 at 8995 eV.

3.2. UV−Vis Diffuse Reflectance. UV−vis confirms the presence of copper species within the zeolite. An intense absorption band is visible in the CZ-WIE and CZ-SSE samples at 200−225 nm (see Figure 3). Previous studies have assigned this feature to the charge transfer between $O^{2-} \rightarrow Cu^{2+}$ or $3d^{10}$−$3d^{9}4s^{1}$ Cu^{+} transitions,[45] although its presence in the copper-free zeolite means that it could also partly be arising as a characteristic transition of the zeolite.[46] The broad absorption band at 800 nm in the CZ-WIE and CZ-SSE is assigned to the d → d transition of isolated distorted octahedral hexa-aqua complexes of Cu^{2+} and has been previously identified in Cu-SSZ-13,[37] Cu-ZSM-5,[47] Cu-SAPO-34,[25] and Cu-BEA.[48]

As the band is broad, it is likely that the absorption band may be due to three different types of Cu^{2+} complexes including divalent complexes charge compensated by an Al pair (e.g., $[Cu(H_2O)_6]^{2+}$), monovalent, single Al charge compensated complexes (e.g., $[Cu\text{-}OH(H_2O)_5]^{+}$), and complexes involving organic ligands. The CZ-SSE exhibits increased absorption in the region between 350 and 620 nm, which can be assigned to charge transfer in O−Cu−O and Cu−O−Cu linear copper systems like CuO.[49] This is also evidenced in the UV−vis studies of copper loading in zeolites where higher copper loadings are accompanied by an increase

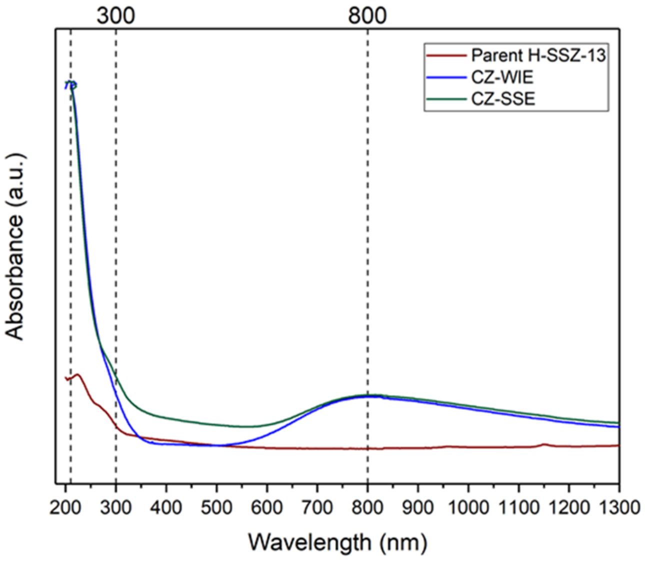

Figure 3. UV−vis of H-SSZ-13 including the blank framework (red), 4× wet ion-exchanged Cu-zeolite (blue), and solid-state exchanged Cu-zeolite (green); data are presented in Kubelka−Munk units, $F(R) = (1 - R)2/2R$, where R is the absolute reflectance of the sampled layer.

in oxidic copper species.[46] CZ-SSE also has a shoulder at around 300 nm that has previously been observed in optical transmission studies of $CuAlO_2$.[49] Overall, the UV−vis data indicate that both samples clearly evidence the presence of copper speciation, with the CZ-SSE clearly exhibiting multiple copper environments.

3.3. Raman Spectroscopy. Raman spectra were acquired for the CZ-WIE, the CZ-SSE, and the copper-free parent zeolite. Representative spectra from five different areas of the sample were acquired and then averaged to create the traces presented in Figure 4. As expected, the copper-free parent SSZ-13 zeolite exhibits the characteristic chabazite SiO_2 peak at 484 cm^{-1}. Like the parent material, the wet ion-exchanged Cu-zeolite preparation shows the strong crystallinity of the chabazite doublet.

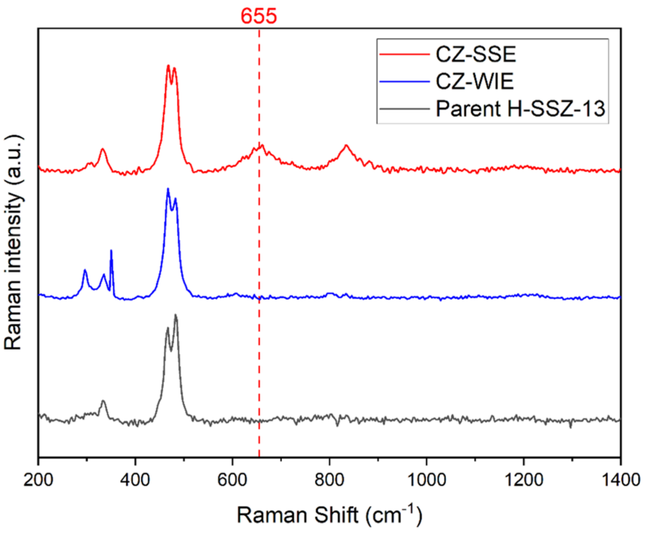

Figure 4. Raman spectra of SSZ-13 including the parent SSZ-13 (black), wet ion-exchanged Cu-zeolite (blue), and solid-state exchanged Cu-zeolite (red) acquired at 830 nm.

The CZ-SSE sample also clearly features the chabazite doublet, indicating that crystallinity is maintained. Two additional bands are also observed in this sample at 655 and 833 cm^{-1}. The band at 833 cm^{-1} has previously been assigned to v_s(T−O−T) stretches[50] of the silicalite structure. However, as this feature is not seen in the other SSZ-13 preparations, it is instead speculated that these peaks may be attributed to a unique copper environment. Previous studies have explored the spectroscopic features of mononuclear and dinuclear Cu_xO_y complexes that might be extant in Cu-zeolite samples. A study by Pappas et al.[51] exploring the structure−activity relationship for Cu-CHA presented Raman data for hydrated and activated Cu-SSZ-13 samples with bands at 510, 580, and 830 cm^{-1} that were assigned to $[Cu(trans\text{-}\mu\text{−}1,2\text{-}O_2)Cu]^{2+}$ species.[52] A shoulder feature is also observed at around 620 cm^{-1}, which could be associated with bis(μ-oxo) dicopper(III) and mono-(μ-oxo) dicopper(II) species.[52−54] Further, Vanelderen et al. showed that such vibrational frequencies can be influenced by the type of framework the molecular copper species are being hosted in.[55] Based on this, it may be reasonable to consider that the band at 830 cm^{-1} could be associated with species featuring an O−O bond and that the band at 655 cm^{-1} could be linked to a Cu−O structure. Nonetheless, our computational work in the following section clarifies the nature of these vibrations.

3.3.1. Raman Simulation. DFT calculations using cluster models of copper incorporated zeolites have been used extensively to add *in silico* backing to observations in Raman spectra.[54,56,57] However, to the best of our knowledge all of these studies have focused on multiple Cu^{2+} sites connected by bridging oxygen(s). Therefore, to assess whether the experimental peaks determined in our data can be attributed to Cu^{1+} aluminate we decided to construct a cluster model including the six-membered ring in which the aluminum substitutes T1 sites. Our model is similar to those used by Artiglia et al.[58] although we include a second layer of the ring system and in all cases terminate by a hydroxyl group (see Figure S6). For our calculations, we construct two models: (1) containing just the aluminum acid site with a proton on the proximal oxygen linker and (2) incorporating all of the atoms of model 1 with the proton substituted for a Cu^+ ion. We observe all four bands found experimentally in the Cu^+-included simulation with the band at 655 cm^{-1} (absent from the protonated model) ascribed to a bending mode of the Al−Cu−O angle. Much of the activity seen in the simulated Raman corresponds to proton waggle modes; however, we can confidently ascribe the important modes seen experimentally to ring motions. After this initial success, we decided to expand these minima models using a multiscale QM/MM protocol. Figure 5 shows the Raman spectra produced using the QM/MM methodology and the eight-membered ring embedded cluster (the results from other clusters are shown in the supporting information (Figures S8 and S9)). Using the embedded cluster approach, the exact position of the Raman peaks is slightly shifted from those found experimentally; however, there are clearly symmetrical and antisymmetrical Al−O−Cu stretch modes (at 603 and 647 cm^{-1}, respectively) and can be assigned to the experimentally observed 655 cm^{-1} peak. For the protonated alternative, the corresponding Al−O−H modes are substantially shifted to 577 and 603 cm^{-1} and are not in good agreement with the experimental spectra. More

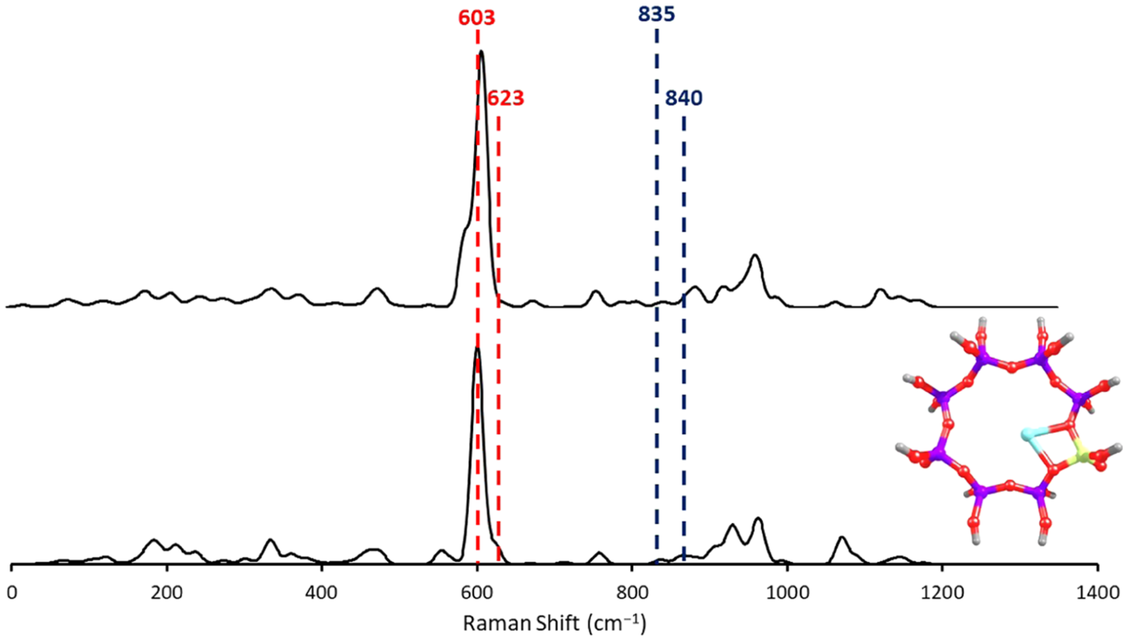

Figure 5. Raman simulation using the QM/MM methodology and the eight-membered ring embedded cluster. Spectra for both the protonated (top) and copper cation containing (bottom) system are depicted with virtual dashed lines included to show the positions of the experimental peaks of interest.

interestingly, there appear to be additional S−Al−O modes at 835 and 840 cm^{-1} that appear in the embedded model, which can be assigned to the experimentally observed Raman activity at 830 cm^{-1}.

3.4. IR Transmission Spectroscopy. To verify if Cu speciation has an influence on formation of N_2O, we examined the catalytic performance of both catalyst samples using IR transmission spectroscopy. NH_3-SCR was performed using a base gas mixture of 1000 ppm NO, 5000 ppm NH_3, and 8000 ppm O_2, which is consistent with the standard conditions used during *operando* NH_3-SCR experiments. IR transmission spectroscopy data in Figure 6 demonstrates noticeably higher N_2O formation on the CZ-SSE catalyst compared to the CZ-WIE catalyst. Information on NO_x conversion of both catalyst samples is shown in Figure S3.

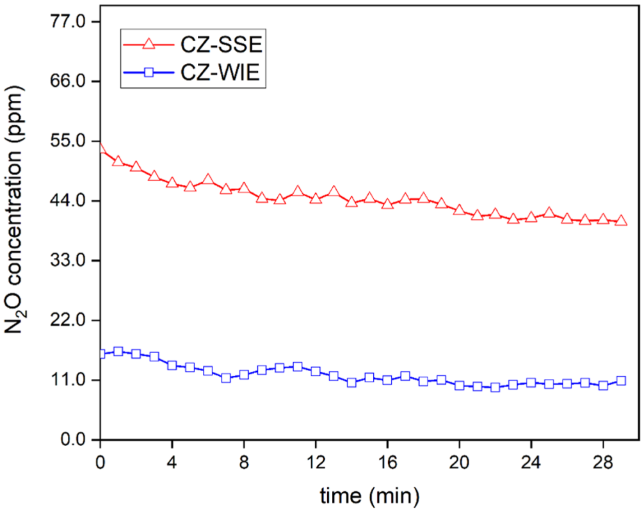

Figure 6. Concentration of N_2O over time upon exposure to NO + O_2 + NH_3 at 250 °C.

3.5. *Operando* Infrared Microspectroscopy. The nature and location of Cu species are influenced by several factors such as the structure of the framework, Si/Al ratios, Cu loadings, and synthesis methods. Furthermore, the oxidation states, location, and the chemical nature of Cu catalytic centers vary as a function of reaction conditions. Hence, only *operando* spectroscopic techniques are capable of monitoring the dynamic behavior of catalysts and establishing accurate structure−function relationships. In this study, we followed the dynamics of reaction using *operando* synchrotron IR microspectroscopy to understand the role of key surface species in the NH_3-SCR reaction and to find their correlation with Cu speciation.

Gas switching experiments were performed to elucidate the formation of surface complexes during NO_x adsorption on the two Cu-zeolite samples. The focus was placed on the region of 1200−2000 cm^{-1} where bands of nitrogen-containing compounds dominate. Figure 7a shows a time series of IR spectra for each Cu-zeolite sample after exposure to NO and O_2 gas at 180 °C. In the region of the IR spectra selected, it is anticipated that the bands emerging are almost exclusively arising out of the interaction between the reactants and copper sites. In both catalyst samples, a series of bands in the region 1500−1650 cm^{-1} are observed soon after introduction of NO + O_2. Bands in this region are typically attributed to surface nitrate groups with different types of co-ordination, which are attributed to the monodentate nitrate linked to Cu sites at 1570 cm^{-1}, monodentate nitrate linked to Al sites at 1602 cm^{-1}, and bridging nitrate based on Al sites at 1625 cm^{-1}.[59−61] Only bridging nitrates were formed on the catalyst surface in the first 5 min followed by bidentate species (Figure 7a). There appears to be a difference in band evolution between each sample, with the bands in the CZ-WIE sample appearing to increase with time and the peak ratios in the CZ-SSE sample appearing to show less variation over a 20 min period.

Figure 7b shows a time series of IR spectra for each Cu-zeolite sample after exposure to NO, O_2, and NH_3 at 180 °C.

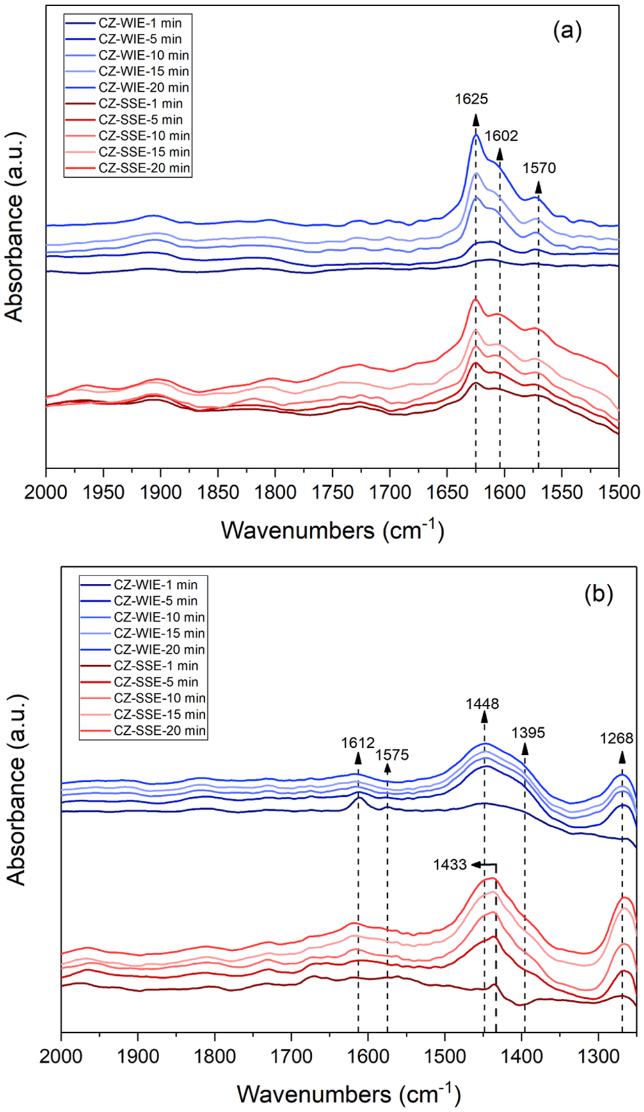

Figure 7. Operando FTIR spectra of Cu-containing SSZ-13 zeolites (CZ-WIE and CZ-SSE) upon exposure to (a) NO + O_2 and (b) NO + O_2 + NH_3 at 180 °C.

The introduction of NH_3 yields the biggest difference in spectra within this region. Nitrate species in the region 1500−1650 cm^{-1} do not appear to exist after exposure to NH_3 indicating their fast consumption by gaseous NH_3. The time series for the CZ-WIE sample is characterized by major band proliferation at 1448 and 1268 cm^{-1}, which both appear following the depletion of a band at 1612 cm^{-1} and are visible immediately after NH_3 exposure but consumed in the 5 min following. The CZ-SSE sample exhibits an even greater response in this region with a more complex ensemble of bands visible at 1268, 1395, 1413, and 1448 cm^{-1}.

Following exposure to NH_3, it is expected that the Cu-containing SSZ-13 zeolites will exhibit bands associated with at least three types of NH_3 adsorbed species.[43] These are (1) ammonium ions formed on Brønsted acid sites still present as a result of incomplete ion-exchange ($\delta(NH_4^+)_{as}$ at 1448 and $\delta(NH_4^+)_s$ at 1395 cm^{-1}),[62−65] (2) $[Cu(NH_3)_4]^{2+}$ complexes arising from NH_3 co-ordination with Cu^{2+} Lewis sites ($\delta(NH_3)_{as}$ at 1612 cm^{-1}) and (3) NH_3 wagging of NH_3 in $[Cu(NH_3)_4]^{2+}$ at 1268 cm^{-1}.[63−66] The absorption of NH_3 (1448 cm^{-1}) on Brønsted acid sites is stronger compared to the Lewis acidic sites (1612 cm^{-1}), which desorbed upon 5 min of reaction in the CZ-WIE catalyst. This has been observed previously by Lezcano-Gonzalez et al. and has been rationalized in terms of NH_4^+ ions reacting more slowly than NH_3 adsorbed on Lewis acid sites.[65] The significant difference between the two samples is the intermediate at 1433 cm^{-1} forming as a result of ammonium interaction with nitrate species that are notably absent in the CZ-WIE sample. This observation is accompanied by the *operando* mass spectroscopy results (see Figure S2) confirming the higher formation of N_2O over the CZ-SSE catalyst compared to the CZ-WIE catalyst under SCR condition, despite both samples exhibiting comparable overall NO_x reduction efficiencies.

While it has been postulated that in Cu-zeolite systems, the N_2O formation mechanism may occur via decomposition of NH_4NO_3 to form N_2O and water especially in the low-temperature region,[22−25] it is proposed that the AlO_2Cu^+ sites within Cu-zeolites act as preferential sites for nitrate formation. With this assumption, we intend to verify if the newly formed intermediate at 1433 cm^{-1} corresponds to the $[SSZ\text{-}13((AlO_2Cu^+)NH_3)NO_3^-]$ structure. The following section focuses on the assignment of peaks from simulated IR spectra that most closely matches post-exposure experimental IR data shown in Figure 7b.

3.6. Simulated IR Spectra. To gain deeper insight into the origin of specific modes as well as to validate our AlO_2Cu^+ active species, *in silico* DFT cluster models and QM/MM embedded clusters of various possible intermediates were constructed. Using the unembedded approach, a comparison between the *in silico* and experimental IR is shown in Figure S7, where the computed analytical frequencies assigned the new feature (at 1420 cm^{-1} in the model) to a NO stretching mode that was softened by the presence of hydrogen bonding to nearby NH_3 molecules. The frequency that corresponds to the NH_3 "wobble" mode was simulated at 1373 cm^{-1}. Using the embedded QM/MM cluster alternative, this NO stretch mode was absent in the 1400−1500 cm^{-1} range when the NO_3^- bound species was considered (see the supporting information, Figure S10). Indeed, this band only reappeared when the bound NO_x species was instead NO_2^- (see Figure 8) with the NH_3 "wobble" mode observed in this embedded cluster at 1241 cm^{-1}.

3.7. Reaction Mechanism toward N_2O. The formation of N_2O from $[SSZ\text{-}13((Cu^+)NH_3)NO_3^-]$ was examined utilizing the periodic DFT methodology. The adsorption of NH_3 and NO_3^- on the $CuAlO_2$ was found to result in proton transfer from the nitrate moiety, giving HNO_3 and NH_3. NO_3 binding to the copper center was deemed to be very stable, whereas NH_4^+ only coordinated Cu^+ after a proton was abstracted by NO_3^-. Therefore, the active $[(Al_2O_4Cu)HNO_3, NH_3]$ intermediate was used as the starting point for the results discussed here. These species are stabilized by hydrogen-bonding interactions at the negative oxygen sites of the zeolite framework. The potential energy landscape shown in Figure 9 explores the thermodynamics of the proposed reaction mechanism. The decomposition of $[SSZ\text{-}13((Cu^+)\text{-}NH_3)HNO_3]$ (1) into N_2O proceeds via sequential dehydration steps. The first dehydration occurs via a proton transfer from NH_3 to the OH moiety of the protonated nitrate group, which produces the H_2N NO_3 intermediate and releases one molecule of water (2). This reaction is endothermic with a formation energy of 1.17 kJ mol^{-1}. After this step, two possible pathways diverge. The pathway for the formation of an early

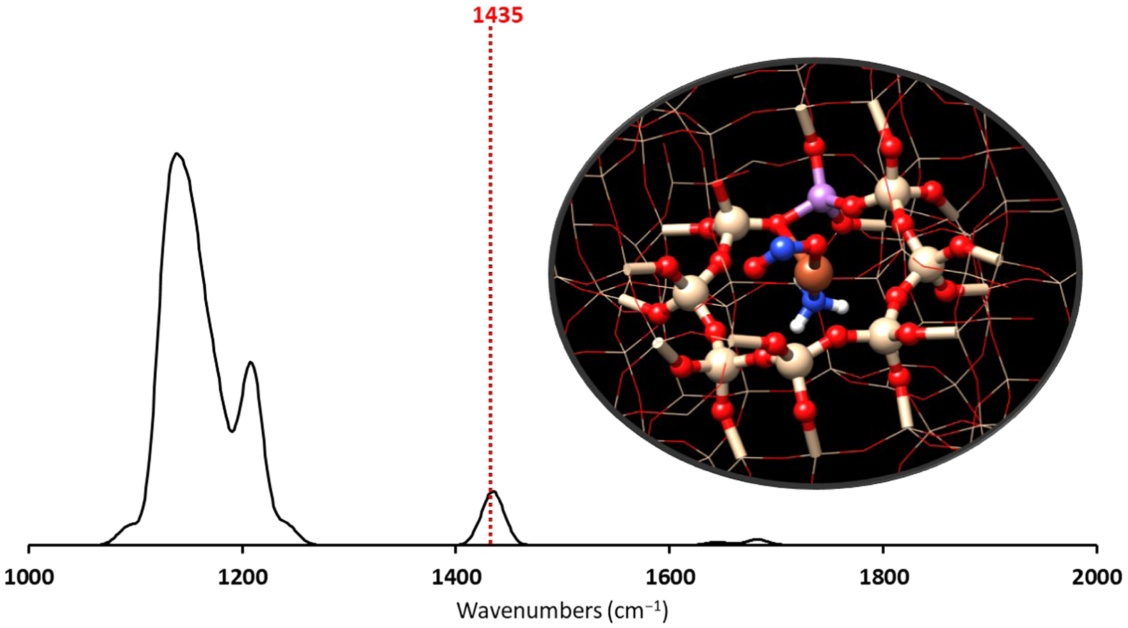

Figure 8. Simulated QM/MM IR spectra of the [SSZ-13((AlO_2Cu^+)NH_3)NO_2^-] model. The model used is shown in the extra framework: Cu (brown), Al (purple), O (red), N (blue), and H (gray) highlighted by a ball and stick depiction, while the framework SiO_2 is shown using a wire framework motif.

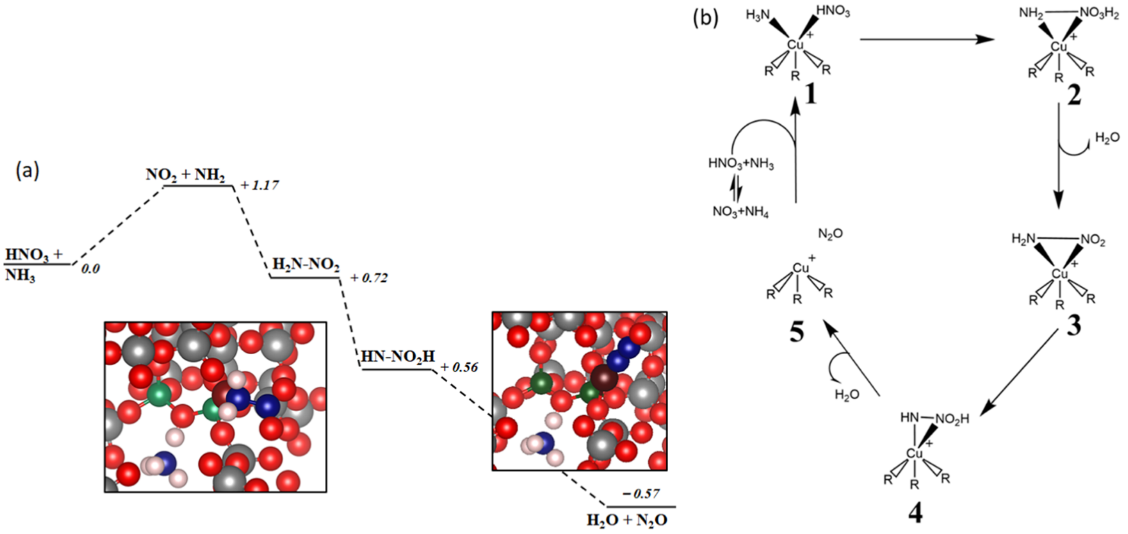

Figure 9. (a) Potential energy surface for the conversion of HNO_3 and NH_3 to NNO and $2H_2O$ by the extra framework $CuAl_2O_3$ in CHA. All energies are given in eV. (b) Proposed mechanisms for the conversion of HNO_3 and NH_3 to NNO and $2H_2O$ by the extra framework $CuAl_2O_3$ in CHA.

NN bond after the first dehydration leads to two intermolecular hydrogen isomerization steps. The thermodynamics of this pathway point to a steady decrease in the energy of the intermediate step until the formation of NNO with a strongly exothermic by ~0.5 eV. The alternative pathway sees the formation of a late NN bond and was calculated to be inaccessible via a NO−Cu−NH intermediate that was >4 eV higher in energy than the reactant (see Figure S11). Our results are in good agreement with the calculated pathways for N_2O production on H-AFX, where an early NN bond formation was also determined to be crucial for effective HNO_3 and NH_3 conversion.[67] Overall, periodic DFT calculations have been used to validate the experimental models and point to the early formation of an NN bound to be critical for a thermodynamically assessable pathway to N_2O formation.

4. CONCLUSIONS

The present findings provide another perspective to elucidate the role of Cu speciation in NH_3-SCR reaction. The data imply that catalyst performance in a reaction might be affected by the synthesis process. Spectroscopic techniques, including *operando* XANES, UV−vis, and Raman, provided indirect evidence for the Cu speciation by detecting changes in the Cu coordination environment. While the XANES indicates the presence of a linear copper species such as $CuAlO_2$, the data generated is not able to comment on what this species might "look" like or how it might be distributed. Given that both samples have been subjected to standard high-temperature activations and gas experiments, it is expected that the Cu(I) species must be stable, making a compound such as an aluminate phase one such possibility. Based on the higher production rate of N_2O, this would also indicate that the species should be readily accessible. By exclusion, a crystalline phase might not constitute a large enough surface area to be considered "readily accessible", meaning it may instead be a disperse species occurrent throughout the sample. Operando IR microspectroscopy pointed to the early formation of a new intermediate along with consumption of nitrate species and adsorption of NH_3 on acid sites; attention should be paid to the Cu local environment that is closely correlated with the evolution of N_2O. According to the DFT calculation results, both the adsorbed NH_4^+ and NO_3^- ions can be associated with $CuAlO_2$ with a similar energy barrier and facilitate the generation of intermediate $[(Al_2O_4Cu)HNO_3, NH_3]$ species during the NH_3-SCR reaction. This may also explain why the presence of a linear copper species such as $CuAlO_2$ significantly influences the local environment of Cu species toward N_2O formation. In this respect, utilizing advanced characterization early in the zeolite preparation process is important to gain a thorough understanding of how the native material originally presents and how it might evolve during the reaction. In a more generic vein, further comparative studies on zeolites prepared in different manners when applied as catalysts might provide further useful insight into the mechanism of NH_3-SCR. The observation of an alternative linear copper species is not limited to the CZ-SSE preparation presented here and may potentially occur in other preparations of Cu-zeolite such as those subjected to aging. These results are part of an ongoing body of research and represent the first stages of characterization. Nonetheless, the detailed understanding of Cu species will help establish more reliable guidelines for developing the NH_3-SCR catalysts or even develop new concepts for optimizing the NH_3-SCR process with Cu species as active sites.

ASSOCIATED CONTENT

Supporting Information

The Supporting Information is available free of charge at https://pubs.acs.org/doi/10.1021/acscatal.1c03174.

> X-ray diffraction (XRD) of Cu-containing SSZ-13 zeolites, N_2 sorption measurements of Cu-containing SSZ-13 zeolites, online activity measurement, scanning electron microscopy (SEM) with energy-dispersive X-ray analysis (EDX) of Cu-containing SSZ-13 zeolites, periodic DFT models, QM/MM Models, DFT cluster methodology (PDF)

AUTHOR INFORMATION

Corresponding Authors

Leila Negahdar − *Chemistry Department, University College of London, London WC1H 0AJ, U.K.; UK Catalysis Hub, Research Complex at Harwell, Rutherford Appleton Laboratory, Didcot OX110FA, U.K.;* orcid.org/0000-0002-9119-6445; Email: l.negahdar@ucl.ac.uk

Andrew M. Beale − *Chemistry Department, University College of London, London WC1H 0AJ, U.K.; Finden Ltd, Abingdon, Oxfordshire OX14 5EG, U.K.; UK Catalysis Hub, Research Complex at Harwell, Rutherford Appleton Laboratory, Didcot OX110FA, U.K.;* Email: andrew.beale@ucl.ac.uk

Authors

Naomi E. Omori − *Chemistry Department, University College of London, London WC1H 0AJ, U.K.; UK Catalysis Hub, Research Complex at Harwell, Rutherford Appleton Laboratory, Didcot OX110FA, U.K.*

Matthew G. Quesne − *School of Chemistry, Cardiff University, Cardiff CF10 3AT, U.K.; UK Catalysis Hub, Research Complex at Harwell, Rutherford Appleton Laboratory, Didcot OX110FA, U.K.;* orcid.org/0000-0001-5130-1266

Mark D. Frogley − *Diamond Light Source Ltd, Harwell Science and Innovation Campus, Didcot OX11 0DE, U.K.*

Fernando Cacho-Nerin − *Diamond Light Source Ltd, Harwell Science and Innovation Campus, Didcot OX11 0DE, U.K.*

Wilm Jones − *Chemistry Department, University College of London, London WC1H 0AJ, U.K.; Finden Ltd, Abingdon, Oxfordshire OX14 5EG, U.K.*

Stephen W. T. Price − *Finden Ltd, Abingdon, Oxfordshire OX14 5EG, U.K.*

C. Richard A. Catlow − *School of Chemistry, Cardiff University, Cardiff CF10 3AT, U.K.; Chemistry Department, University College of London, London WC1H 0AJ, U.K.; UK Catalysis Hub, Research Complex at Harwell, Rutherford Appleton Laboratory, Didcot OX110FA, U.K.;* orcid.org/0000-0002-1341-1541

Complete contact information is available at: https://pubs.acs.org/10.1021/acscatal.1c03174

Notes

The authors declare no competing financial interest.

ACKNOWLEDGMENTS

L. N. has received funding from the European Union's Horizon 2020 research and innovation programme under the Marie Skłodowska-Curie grant agreement No. 837794. "This work was carried out with the support of Diamond Light Source, reference: SM22298−1, Instrument: B22 and I14. ISIS Pulsed Neutron and Muon Source is greatly thanked for performing XRD measurements. The UK Catalysis Hub is kindly thanked for the resources and support provided via membership of the UK Catalysis Hub Consortium and funded by EPSRC (portfolio grants EP/K014706/1, EP/K014668/1, EP/K014854/1, EP/K014714/1, and EP/I019693/1). W. J., A. M. B., and S. W. T. P thank Innovate UK project number 104253 for financial support. Dr. Ines. Lezcano-Gonzalez and Dr. Alex G. Greenaway are greatly thanked for preparing the catalyst samples.

REFERENCES

(1) Mauzerall, D. L.; Sultan, B.; Kim, N.; Bradford, D. F. NO_x Emissions from Large Point Sources: Variability in Ozone Production, Resulting Health Damages and Economic Costs. *Atmos. Environ.* **2005**, *39*, 2851−2866.

(2) European Environment Agency. *European Union Emission Inventory Report 1990-2011 under the UNECE Convention on Long-Range Transboundary Air Pollution (LRTAP)*, 2013.

(3) Radhamohan, S.; Crane, M. E. Multistage Reductant Injection Strategy for Slipless, High Efficiency Selective Catalytic Reduction. U.S. Patent US69969752006.

(4) Deka, U.; Juhin, A.; Eilertsen, E. A.; Emerich, H.; Green, M. A.; Korhonen, S. T.; Weckhuysen, B. M.; Beale, A. M. Confirmation of Isolated Cu 2+ Ions in SSZ-13 Zeolite as Active Sites in NH 3-

Selective Catalytic Reduction. *J. Phys. Chem. C* **2012**, *116*, 4809−4818.

(5) Ma, L.; Cheng, Y.; Cavataio, G.; McCabe, R. W.; Fu, L.; Li, J. Characterization of Commercial Cu-SSZ-13 and Cu-SAPO-34 Catalysts with Hydrothermal Treatment for NH3-SCR of NOx in Diesel Exhaust. *Chem. Eng. J.* **2013**, *225*, 323−330.

(6) Beale, A. M.; Gao, F.; Lezcano-Gonzalez, I.; Peden, C. H. F.; Szanyi, J. Recent Advances in Automotive Catalysis for NOx Emission Control by Small-Pore Microporous Materials. *Chem. Soc. Rev.* **2015**, *44*, 7371−7405.

(7) Fu, M.; Li, C.; Lu, P.; Qu, L.; Zhang, M.; Zhou, Y.; Yu, M.; Fang, Y. A Review on Selective Catalytic Reduction of NOx by Supported Catalysts at 100−300 °C—Catalysts, Mechanism, Kinetics. *Catal. Sci. Technol.* **2014**, *4*, 14−25.

(8) Damma, D.; Ettireddy, P. R.; Reddy, B. M.; Smirniotis, P. G. A Review of Low Temperature NH 3 -SCR for Removal of NO X. *Catalysts* **2019**, 349.

(9) Shan, Y.; Shi, X.; Du, J.; Yu, Y.; He, H. Cu-Exchanged RTH-Type Zeolites for NH3-Selective Catalytic Reduction of NOx: Cu Distribution and Hydrothermal Stability. *Catal. Sci. Technol.* **2019**, *9*, 106−115.

(10) Chen, H.-Y. Cu/Zeolite SCR Catalysts for Automotive Diesel NOx Emission Control. In *Urea-SCR Technology for deNOX after Treatment of Diesel Exhausts*; Springer: New York, NY, 2014.

(11) Zhang, D.; Yang, R. T. N2O Formation Pathways over Zeolite-Supported Cu and Fe Catalysts in NH3-SCR. *Energy Fuels* **2018**, *32*, 2170−2182.

(12) Liu, B.; Yao, D.; Wu, F.; Wei, L.; Li, X.; Wang, X. Experimental Investigation on N2O Formation during the Selective Catalytic Reduction of NOx with NH3 over Cu-SSZ-13. *Ind. Eng. Chem. Res.* **2019**, *58*, 20516−20527.

(13) Kamasamudram, K.; Henry, C.; Currier, N.; Yezerets, A. N2O Formation and Mitigation in Diesel Aftertreatment Systems. *SAE Int. J. Engines* **2012**, *5*, 688−698.

(14) Shin, Y.; Jung, Y.; Cho, C. P.; Pyo, Y. D.; Jang, J.; Kim, G.; Kim, T. M. NOx Abatement and N2O Formation over Urea-SCR Systems with Zeolite Supported Fe and Cu Catalysts in a Nonroad Diesel Engine. *Chem. Eng. J.* **2020**, *381*, No. 122751.

(15) Yang, S.; Xiong, S.; Liao, Y.; Xiao, X.; Qi, F.; Peng, Y.; Fu, Y.; Shan, W.; Li, J. Mechanism of N2O Formation during the Low-Temperature Selective Catalytic Reduction of NO with NH3 over Mn-Fe Spinel. *Environ. Sci. Technol.* **2014**, *48*, 10354−10362.

(16) Yates, M.; Martín, J. A.; Martín-Luengo, M. Á.; Suárez, S.; Blanco, J. N2O Formation in the Ammonia Oxidation and in the SCR Process with V2O5-WO3 Catalysts. *Catal. Today* **2005**, *107−108*, 120−125.

(17) Zhang, B.; Liebau, M.; Suprun, W.; Liu, B.; Zhang, S.; Gläser, R. Suppression of N2O Formation by H2O and SO2 in the Selective Catalytic Reduction of NO with NH3 over a Mn/Ti−Si Catalyst. *Catal. Sci. Technol.* **2019**, *9*, 4759−4770.

(18) Yagiela, J. A. Health Hazards and Nitrous Oxide: A Time for Reappraisal. *Anaesth. Prog.* **1991**, *38*, 1−11.

(19) Forster, P.; Ramaswamy, V.; Artaxo, P.; Berntsen, T.; Betts, R.; Fahey, D. W.; Haywood, J.; J, L.; Lowe, D. C.; Myhre, G.; Nganga, J.; Prinn, R.; Raga, G.; Schulz, M.; Van Dorland, R. Changes in Atmospheric Constituents and in Radiative Forcing. In *Climate Change 2007: The Physical Science Basis. Contribution of Working Group I to the Fourth Assessment Report of the Intergovernmental Panel on Climate Change*; Cambridge University Press: Cambridge, 2007.

(20) Wang, J.; Cui, H.; Dong, X.; Zhao, H.; Wang, Y.; Chen, H.; Yao, M.; Li, Y. N2O Formation in the Selective Catalytic Reduction of NOx with NH3 on a CeMoOx Catalyst. *Appl. Catal., A* **2015**, *505*, 8−15.

(21) Brandenberger, S.; Kröcher, O.; Tissler, A.; Althoff, R. The State of the Art in Selective Catalytic Reduction of NOx by Ammonia Using Metal-Exchanged Zeolite Catalysts. *Catal. Rev.: Sci. Eng.* **2008**, 492−531.

(22) Kwak, J. H.; Tran, D.; Szanyi, J.; Peden, C. H. F.; Lee, J. H. The Effect of Copper Loading on the Selective Catalytic Reduction of Nitric Oxide by Ammonia over Cu-SSZ-13. *Catal. Lett.* **2012**, *142*, 295−301.

(23) Centi, G.; Perathoner, S.; Biglino, D.; Giamello, E. Adsorption and Reactivity of NO on Copper-on-Alumina Catalysts: I. Formation of Nitrate Species and Their Influence on Reactivity in No and NH3 Conversion. *J. Catal.* **1995**, *152*, 75−92.

(24) Gao, F.; Kwak, J. H.; Szanyi, J.; Peden, C. H. F. Current Understanding of Cu-Exchanged Chabazite Molecular Sieves for Use as Commercial Diesel Engine DeNOx Catalysts. *Top. Catal.* **2013**, *56*, 1441−1459.

(25) Leistner, K.; Brüsewitz, F.; Wijayanti, K.; Kumar, A.; Kamasamudram, K.; Olsson, L. Impact of Copper Loading on Nh3-Selective Catalytic Reduction, Oxidation Reactions and N2O Formation over Cu/SAPO-34. *Energies* **2017**, *10*, 489.

(26) Kwak, J. H.; Tran, D.; Burton, S. D.; Szanyi, J.; Lee, J. H.; Peden, C. H. F. Effects of Hydrothermal Aging on NH 3-SCR Reaction over Cu/Zeolites. *J. Catal.* **2012**, *287*, 203−209.

(27) Lee, J. H.; Kim, Y. J.; Ryu, T.; Kim, P. S.; Kim, C. H.; Hong, S. B. Synthesis of Zeolite UZM-35 and Catalytic Properties of Copper-Exchanged UZM-35 for Ammonia Selective Catalytic Reduction. *Appl. Catal., B* **2017**, *200*, 428−438.

(28) Gao, F.; Walter, E. D.; Washton, N. M.; Szanyi, J.; Peden, C. H. F. Synthesis and Evaluation of Cu-SAPO-34 Catalysts for Ammonia Selective Catalytic Reduction. 1. Aqueous Solution Ion Exchange. *ACS Catal.* **2013**, *3*, 2083−2093.

(29) Deka, U.; Lezcano-Gonzalez, I.; Weckhuysen, B. M.; Beale, A. M. Local Environment and Nature of Cu Active Sites in Zeolite-Based Catalysts for the Selective Catalytic Reduction of NOx. *ACS Catal.* **2013**, *3*, 413−427.

(30) Deka, U.; Lezcano-Gonzalez, I.; Warrender, S. J.; Lorena Picone, A.; Wright, P. A.; Weckhuysen, B. M.; Beale, A. M. Changing Active Sites in Cu-CHA Catalysts: DeNO x Selectivity as a Function of the Preparation Method. *Microporous Mesoporous Mater.* **2013**, 144−152.

(31) Schmidt, J. E.; Oord, R.; Guo, W.; Poplawsky, J. D.; Weckhuysen, B. M. Nanoscale Tomography Reveals the Deactivation of Automotive Copper-Exchanged Zeolite Catalysts. *Nat. Commun.* **2017**, *8*, No. 1666.

(32) Moliner, M.; Franch, C.; Palomares, E.; Grill, M.; Corma, A. Cu-SSZ-39, an Active and Hydrothermally Stable Catalyst for the Selective Catalytic Reduction of NOx. *Chem. Commun.* **2012**, *48*, 8264−8266.

(33) Beale, A. M.; Lezcano-Gonzalez, I.; Slawinksi, W. A.; Wragg, D. S. Correlation between Cu Ion Migration Behaviour and DeNOx Activity in Cu-SSZ-13 for the Standard NH3-SCR Reaction. *Chem. Commun.* **2016**, *52*, 6170.

(34) Greenaway, A. G.; Lezcano-Gonzalez, I.; Agote-Aran, M.; Gibson, E. K.; Odarchenko, Y.; Beale, A. M. Operando Spectroscopic Studies of Cu−SSZ-13 for NH3−SCR DeNOx Investigates the Role of NH3in Observed Cu(II) Reduction at High NO Conversions. *Top. Catal.* **2018**, *61*, 175−182.

(35) Peña, F. d.; Prestat, E.; Fauske, V. T.; Burdet, P.; Jokubauskas, P.; Nord, M.; Ostasevicius, T.; MacArthur, K. E.; Sarahan, M.; Johnstone, D. N.; Taillon, J.; Lähnemann, J.; Migunov, V.; Eljarrat, A.; Caron, J.; Aarholt, T.; Mazzucco, S.; Walls, M.; Slater, T.; Winkler, F.; pquinn-dls Martineau, B.; Donval, G.; McLeod, R.; Hoglund, E. R.; Alxneit, I.; Lundeby, D.; Henninen, T.; Zagonel, L. F.; Garmannslund, A. Hyperspy/Hyperspy: HyperSpy v1.5.2. *Zenodo* **2019**. DOI: 10.5281/ZENODO.3396791.

(36) Peña, F. d.; Fauske, V. T.; Burdet, P.; Prestat, E.; Jokubauskas, P.; Nord, M.; Skorikov, A.; et al.*Hyperspy/hyperspy*, version v1. 4.1; Zenodo: Meyrin, Switzerland, 2018.

(37) Bates, S. A.; Verma, A. A.; Paolucci, C.; Parekh, A. A.; Anggara, T.; Yezerets, A.; Schneider, W. F.; Miller, J. T.; Delgass, W. N.; Ribeiro, F. H. Identification of the Active Cu Site in Standard Selective Catalytic Reduction with Ammonia on Cu-SSZ-13. *J. Catal.* **2014**, *312*, 87−97.

(38) Sherwood, P. *ChemShell, a Computational Chemistry Shell*, 2013.

(39) Lu, Y.; Farrow, M. R.; Fayon, P.; Logsdail, A. J.; Sokol, A. A.; Catlow, C. R. A.; Sherwood, P.; Keal, T. W. Open-Source, Python-Based Redevelopment of the ChemShell Multiscale QM/MM Environment. *J. Chem. Theory Comput.* **2019**, *15*, 1317−1328.

(40) Nastase, S. A. F.; O'Malley, A. J.; Catlow, C. R. A.; Logsdail, A. J. Computational QM/MM Investigation of the Adsorption of MTH Active Species in H-Y and H-ZSM-5. *Phys. Chem. Chem. Phys.* **2019**, *21*, 2639−2650.

(41) O'Malley, A. J.; Logsdail, A. J.; Sokol, A. A.; Catlow, C. R. A. Modelling Metal Centres, Acid Sites and Reaction Mechanisms in Microporous Catalysts. *Faraday Discuss.* **2016**, *188*, 235−255.

(42) Durá, O. J.; Boada, R.; Rivera-Calzada, A.; León, C.; Bauer, E.; De La Torre, M. A. L.; Chaboy, J. Transport, Electronic, and Structural Properties of Nanocrystalline CuAlO2 Delafossites. *Phys. Rev. B: Condens. Matter Mater. Phys.* **2011**, *83*, No. 045202.

(43) Lezcano-Gonzalez, I.; Wragg, D. S.; Slawinski, W. A.; Hemelsoet, K.; Van Yperen-De Deyne, A.; Waroquier, M.; Van Speybroeck, V.; Beale, A. M. Determination of the Nature of the Cu Coordination Complexes Formed in the Presence of NO and NH3 within SSZ-13. *J. Phys. Chem. C* **2015**, *119*, 24393−24403.

(44) Greenaway, A. G.; Lezcano-Gonzalez, I.; Agote-Aran, M.; Gibson, E. K.; Odarchenko, Y.; Beale, A. M. Operando Spectroscopic Studies of Cu−SSZ-13 for NH3−SCR DeNOx Investigates the Role of NH3 in Observed Cu(II) Reduction at High NO Conversions. *Top. Catal.* **2018**, *61*, 175−182.

(45) Clemens, A. K. S.; Shishkin, A.; Carlsson, P. A.; Skoglundh, M.; Martínez-Casado, F. J.; Matej, Z.; Balmes, O.; Härelind, H. Reaction-Driven Ion Exchange of Copper into Zeolite SSZ-13. *ACS Catal.* **2015**, *5*, 6209−6218.

(46) Leistner, K.; Xie, K.; Kumar, A.; Kamasamudram, K.; Olsson, L. Ammonia Desorption Peaks Can Be Assigned to Different Copper Sites in Cu/SSZ-13. *Catal. Lett.* **2017**, *147*, 1882−1890.

(47) Dědeček, J.; Wichterlová, B. Role of Hydrated Cu Ion Complexes and Aluminum Distribution in the Framework on the Cu Ion Siting in ZSM-5. *J. Phys. Chem. B* **1997**, *101*, 10233−10240.

(48) Wilken, N.; Nedyalkova, R.; Kamasamudram, K.; Li, J.; Currier, N. W.; Vedaiyan, R.; Yezerets, A.; Olsson, L. Investigation of the Effect of Accelerated Hydrothermal Aging on the Cu Sites in a Cu-BEA Catalyst for NH3-SCR Applications. *Top. Catal.* **2013**, 317−332.

(49) Akyildiz, H. Synthesis of CuAlO2 from Chemically Precipitated Nano-Sized Precursors. *Ceram. Int.* **2015**, *41*, 14108−14115.

(50) Miecznikowski, A.; Hanuza, J. Infrared and Raman Studies of ZSM-5 and Silicalite-1 at Room, Liquid Nitrogen and Helium Temperatures. *Zeolites* **1987**, *7*, 249−254.

(51) Pappas, D. K.; Borfecchia, E.; Dyballa, M.; Pankin, I. A.; Lomachenko, K. A.; Martini, A.; Signorile, M.; Teketel, S.; Arstad, B.; Berlier, G.; Lamberti, C.; Bordiga, S.; Olsbye, U.; Lillerud, K. P.; Svelle, S.; Beato, P. Methane to Methanol: Structure-Activity Relationships for Cu-CHA. *J. Am. Chem. Soc.* **2017**, *139*, 14961−14975.

(52) Ipek, B.; Wulfers, M. J.; Kim, H.; Göltl, F.; Hermans, I.; Smith, J. P.; Booksh, K. S.; Brown, C. M.; Lobo, R. F. Formation of [Cu2O2]2+ and [Cu2O]2+ toward C-H Bond Activation in Cu-SSZ-13 and Cu-SSZ-39. *ACS Catal.* **2017**, *7*, 4291−4303.

(53) Henson, M. J.; Mukherjee, P.; Root, D. E.; Stack, T. D. P.; Solomon, E. I. Spectroscopic and Electronic Structural Studies of the Cu(III)2 Bis-μ- Oxo Core and Its Relation to the Side-on Peroxo-Bridged Dimer. *J. Am. Chem. Soc.* **1999**, *121*, 10332−10345.

(54) Woertink, J. S.; Smeets, P. J.; Groothaert, M. H.; Vance, M. A.; Sels, B. F.; Schoonheydt, R. A.; Solomon, E. I. A [Cu2O]2+ Core in Cu-ZSM-5, the Active Site in the Oxidation of Methane to Methanol. *Proc. Natl. Acad. Sci. USA* **2009**, *106*, 18908−18913.

(55) Vanelderen, P.; Snyder, B. E. R.; Tsai, M. L.; Hadt, R. G.; Vancauwenbergh, J.; Coussens, O.; Schoonheydt, R. A.; Sels, B. F.; Solomon, E. I. Spectroscopic Definition of the Copper Active Sites in Mordenite: Selective Methane Oxidation. *J. Am. Chem. Soc.* **2015**, *137*, 6383−6392.

(56) Vanelderen, P.; Hadt, R. G.; Smeets, P. J.; Solomon, E. I.; Schoonheydt, R. A.; Sels, B. F. Cu-ZSM-5: A Biomimetic Inorganic Model for Methane Oxidation. *J. Catal.* **2011**, *284*, 157−164.

(57) Vogiatzis, K. D.; Li, G.; Hensen, E. J. M.; Gagliardi, L.; Pidko, E. A. Electronic Structure of the [Cu3(μ-O)3]2+ Cluster in Mordenite Zeolite and Its Effects on the Methane to Methanol Oxidation. *J. Phys. Chem. C* **2017**, *121*, 22295−22302.

(58) Artiglia, L.; Sushkevich, V. L.; Palagin, D.; Knorpp, A. J.; Roy, K.; Van Bokhoven, J. A. In Situ X-Ray Photoelectron Spectroscopy Detects Multiple Active Sites Involved in the Selective Anaerobic Oxidation of Methane in Copper-Exchanged Zeolites. *ACS Catal.* **2019**, *9*, 6728−6737.

(59) Long, R. Q.; Yang, R. T. Reaction Mechanism of Selective Catalytic Reduction of NO with NH3 over Fe-ZSM-5 Catalyst. *J. Catal.* **2002**, *207*, 224−231.

(60) Skarlis, S. A.; Berthout, D.; Nicolle, A.; Dujardin, C.; Granger, P. Combined IR Spectroscopy and Kinetic Modeling of NOx Storage and NO Oxidation on Fe-BEA SCR Catalysts. *Appl. Catal., B* **2014**, *148−149*, 446−465.

(61) Ruggeri, M. P.; Grossale, A.; Nova, I.; Tronconi, E.; Jirglova, H.; Sobalik, Z. FTIR in Situ Mechanistic Study of the NH 3NO/NO 2 "Fast SCR" Reaction over a Commercial Fe-ZSM-5 Catalyst. *Catal. Today* **2012**, 107−114.

(62) Suzuki, K.; Sastre, G.; Katada, N.; Niwa, M. Ammonia IRMS-TPD Measurements and DFT Calculation on Acidic Hydroxyl Groups in CHA-Type Zeolites. *Phys. Chem. Chem. Phys.* **2007**, *9*, 5980−5987.

(63) Elzey, S.; Mubayi, A.; Larsen, S. C.; Grassian, V. H. FTIR Study of the Selective Catalytic Reduction of NO2 with Ammonia on Nanocrystalline NaY and CuY. *J. Mol. Catal. A: Chem.* **2008**, *285*, 48−57.

(64) Jentys, A.; Warecka, G.; Lercher, J. A. Surface Chemistry of H-ZSM5 Studied by Time-Resolved IR Spectroscopy. *J. Mol. Catal.* **1989**, *51*, 309−327.

(65) Lezcano-Gonzalez, I.; Deka, U.; Arstad, B.; Van Yperen-De Deyne, A.; Hemelsoet, K.; Waroquier, M.; Van Speybroeck, V.; Weckhuysen, B. M.; Beale, A. M. Determining the Storage, Availability and Reactivity of NH3 within Cu-Chabazite-Based Ammonia Selective Catalytic Reduction Systems. *Phys. Chem. Chem. Phys.* **2014**, *16*, 1639.

(66) Howard, J.; Nicol, J. M. Fourier-Transform Infrared Studies of Copper-Containing Y Zeolites. Dehydration, Reduction and the Adsorption of Ammonia. *J. Chem. Soc., Faraday Trans. 1* **1989**, *85*, 1233−1244.

(67) Kubota, H.; Liu, C.; Toyao, T.; Maeno, Z.; Ogura, M.; Nakazawa, N.; Inagaki, S.; Kubota, Y.; Shimizu, K. I. Formation and Reactions of NH4NO3 during Transient and Steady-State NH3-SCR of NOx over H-AFX Zeolites: Spectroscopic and Theoretical Studies. *ACS Catal.* **2020**, *10*, 2334−2344.